Integrating Climate Change into Hydraulic Hazard Assessment: A Comprehensive Two-Dimensional Modeling Approach on the Muto Stream Basin

Analysis based on the methodologies by Biagio Saya

July 30, 2026

Abstract

The Mediterranean basin is currently experiencing a profound shift in its climatological baseline, with extreme weather events striking coastal and inland catchments with unprecedented intensity. This changing paradigm forces engineers, hydrologists, and environmental planners to fundamentally rethink how spatial management and infrastructure design are approached. In this paper, we document and test a comprehensive methodology specifically tailored for high-risk, ungauged catchments. The primary study area is the Torrente Muto watershed, along with its highly responsive tributaries. By tightly coupling regional precipitation statistical analysis, modern climate change amplification factors, the SCS-CN hydrologic methodology, and advanced two-dimensional hydrodynamic routing (via HEC-RAS 2D), we successfully bridged the gap between theoretical atmospheric forecasting and high-resolution hydraulic hazard zoning. We present the mathematical formulations, assumptions, and GIS-based operational workflows that allow this framework to function as a legally defensible tool for hydrogeological safeguarding and urban planning in vulnerable territories.

Contents

1 Introduction

Managing flood risk in Mediterranean river networks is notoriously difficult, representing one of the most pressing environmental challenges in Southern Europe. These catchments are usually defined by steep topographies, ephemeral streams, and extremely short times of concentration. When heavy rainfall hits, the physical response of the basin is almost immediate, transforming dry riverbeds into torrential flows that frequently overwhelm downstream urban infrastructure [5]. The Torrente Muto basin is a perfect example of this dynamic, characterized by a rapid topographic drop from its mountainous headwaters to the heavily anthropized coastal plain.

To compound an already difficult engineering problem, recent climate trends have introduced a distinct non-stationarity into precipitation patterns. High-intensity, short-duration storm events—often termed "flash floods" or "cloudbursts"—are rapidly becoming the new normal [9]. These extreme occurrences are frequently driven by localized convective systems that dump massive volumes of water over small areas, leaving virtually no warning time for civil protection agencies. This climatic shift is dangerously coupled with decades of intense anthropogenic pressure. Rapid urbanization, extensive soil sealing, and the encroachment of residential areas into historical floodplains have drastically reduced the natural infiltration capacity of these basins.

For decades, hydraulic engineers relied on historical, stationary datasets to design bridges, culverts, and levee systems, implicitly assuming that the statistical properties of past rainfall would hold true for the future. That assumption of stationarity is now largely invalid [13]. As the frequency of extreme events increasingly exceeds the design thresholds of legacy infrastructure, the vulnerability of these territories grows exponentially.

Furthermore, standard one-dimensional (1D) modeling, which solves the energy equation along a single predefined streamline, simply cannot map the complex realities of an urban flood. While computationally efficient, 1D models fail to accurately simulate flow bifurcations, stagnant zones, street-level routing, or the localized hydraulic bottlenecks caused by complex built environments [**?**]. In dense urban matrices, floodwaters rarely follow a single channelized path; instead, they propagate laterally, interacting dynamically with buildings, walls, and road networks. Achieving a reliable, realistic hazard assessment today demands high-fidelity, two-dimensional (2D) hydrodynamic models. By solving the Shallow Water Equations (SWE) over a continuous topographic mesh, these models provide a spatially distributed representation of water depths and velocities. Crucially, these models must be driven by updated meteorological forcing that explicitly accounts for climate change adaptation factors.

To demonstrate the viability of this modern approach, we structured our research around the Torrente Muto catchment. This basin covers approximately 39 km^2 and features a main channel length of roughly 14.5 km. The analysis wouldn't be complete without examining its smaller, highly critical sub-basins: Canalicchio (3.11 km^2), Belvedere (0.76 km^2), and Pintarca (1.14 km^2). These sub-catchments represent the "headwaters of risk"—steep, localized areas where runoff concentrates violently before hitting the main stem. The highly responsive nature of these tributaries dictates the overall flood wave dynamics of the Muto system, making their accurate hydrological parameterization vital for downstream safety.

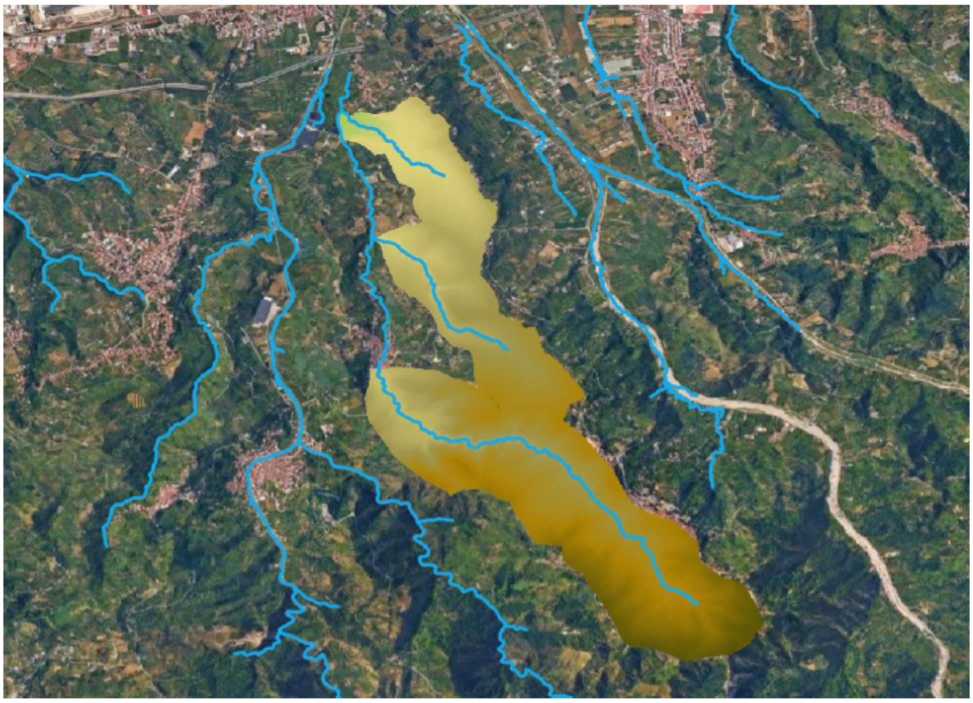

Figure 1: Geographical overview and delimitation of the Torrente Muto basin and its main tributaries, overlaid on high-resolution satellite imagery.

The core philosophy of this study relies heavily on interoperability and the integration of open-source and industry-standard tools [11, 12]. By exploiting the seamless exchange of spatial data between QGIS (utilized for advanced morphometric extraction, land-use processing, and hydrological pre-processing) and the HEC-RAS 2D engine (for rigorous computational fluid dynamics), we outline a comprehensive, reproducible workflow. This methodology moves logically from raw probabilistic rainfall forecasting—incorporating climate non-stationarity—through event-based rainfall-runoff transformations, all the way to detailed, actionable hazard zoning. Ultimately, this framework aims to bridge the gap between theoretical climate science and practical, legally defensible territorial planning.

2 Hydrological Framework and Climate Non-Stationarity

The foundation of any hydraulic model is the hydrological input. If the hydrograph is flawed, the resulting hazard maps will be virtually useless, regardless of how detailed the 2D mesh is [11, 12]. Dealing with an ungauged basin like the Muto requires a rigorous statistical approach to regionalize rainfall data and synthesize design storms [11]. In the absence of direct hydrometric monitoring networks, the engineering challenge shifts toward translating statistical rainfall quantiles into realistic surface runoff hydrographs while minimizing predictive uncertainty [3].

This task is further complicated by the manifestation of climate non-stationarity in the Mediterranean basin [13]. Historical records can no longer be assumed to represent a static statistical distribution. Instead, warming atmospheric temperatures increase the water vapor holding capacity—governed by the Clausius-Clapeyron relation—leading to highly convective, severe precipitation anomalies. To build territorial resilience, the hydrological framework must explicitly bridge classic extreme value theory with modern climate adaptation indices.

2.1 Extreme Value Statistics and DDF Estimation

To characterize the rainfall regime of the study area, we analyzed annual maximum precipitation series from surrounding regional rain gauges for standard durations: 1, 3, 6, 12, and 24 hours. Following a rigorous screening and quality control process, the Gumbel (Extreme Value Type I) distribution proved to be particularly suitable for modeling the probability of exceedance across these short durations. The cumulative distribution function for the Gumbel law, expressing the non-exceedance probability $P(x)$, is defined as:

$$P(x) = \exp\left\{-\exp\left[-\frac{x-u_d}{\alpha_d}\right]\right\} \tag{1}$$

where α_d is the scale parameter (linked to sample dispersion) and u_d is the location parameter (representing the mode of the distribution).

To ensure statistical robustness and minimize the bias associated with short historical records, the selection of parameters followed a comparative framework between the standard Method of Moments (MoM) and the Method of L-Moments

[8]. When applying the Method of Moments, the parameters are directly coupled to the sample mean (m_d), standard deviation (σ_d), and coefficient of variation ($C_{vd} = \sigma_d/m_d$), leading to the following expressions:

$$\alpha_d = \frac{\sqrt{6}}{\pi}\sigma_d \approx 0.7797 \cdot \sigma_d = 0.7797 \cdot m_d \cdot C_{vd} \tag{2}$$

$$u_d = m_d - \gamma \cdot \alpha_d \approx m_d - 0.5772 \cdot \alpha_d \approx m_d \cdot (1 - 0.4501 \cdot C_{vd}) \tag{3}$$

where $\gamma \approx 0.5772$ is the Euler-Mascheroni constant.

Once the location and scale parameters are fixed for each target duration d, the inverse cumulative distribution function (quantile function) is exploited to compute the design precipitation depth x_T for any specific target return period T. By definition, the return period is related to the non-exceedance probability by $P(x_T) = 1 - 1/T$. Substituting this relation into the Gumbel formulation yields the frequency factor equation:

$$x_T = u_d - \alpha_d \cdot \ln\left[-\ln\left(1 - \frac{1}{T}\right)\right] \tag{4}$$

By fitting these calculated quantiles across the entire duration spectrum ($d = 1, 3, 6, 12, 24$ hours), we establish the baseline Depth-Duration-Frequency (DDF) curves, expressed in the standard two-parameter power-law form:

$$h(t, T) = a(T) \cdot t^n \tag{5}$$

where h is the cumulative rainfall depth (mm), t is the storm duration (hours), n is the regional geomorphological scaling exponent—assumed to be constant for a specific homogeneous meteorological zone—while $a(T)$ is the return period-dependent scaling coefficient. The parameter $a(T)$ encapsulates the climatic forcing and exhibits an explicit functional dependence on T, typically mapped via a secondary Gumbel-derived regression:

$$a(T) = a_1 \cdot \left[1 + b_1 \cdot \ln\left(-\ln\left(1 - \frac{1}{T}\right)\right)\right] \tag{6}$$

where a_1 and b_1 are localized regression constants.

The systematic sequence required to operationalize this hydrological framework—moving from raw gauge observations to the final mathematical formulation of the DDF curves—is detailed in the operational workflow below (Figure 2).

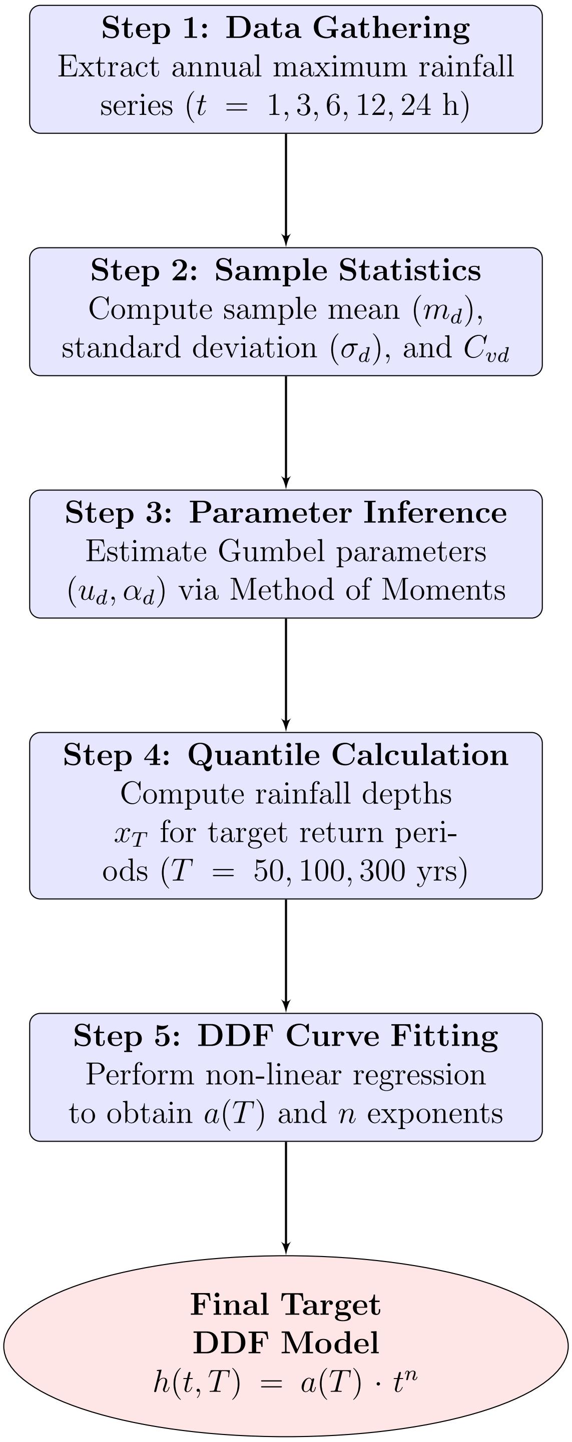

Figure 2: Methodological flowchart for rainfall data regionalization and mathematical synthesis of Depth-Duration-Frequency (DDF) curves.

2.2 Extreme Value Statistics and DDF Estimation

Because local flow gauges were either non-existent or lacked a sufficiently long historical record, our first major task was establishing reliable Depth-Duration-Frequency

(DDF) or Rainfall Probability Curves (RPC). We collected and analyzed annual maximum precipitation series from surrounding regional rain gauges for standard durations: 1, 3, 6, 12, and 24 hours.

Before fitting any distribution, the raw datasets underwent a meticulous screening process to identify and manage outliers, which can severely skew the tails of statistical distributions. We visually and quantitatively assessed the dispersion of these extreme values.

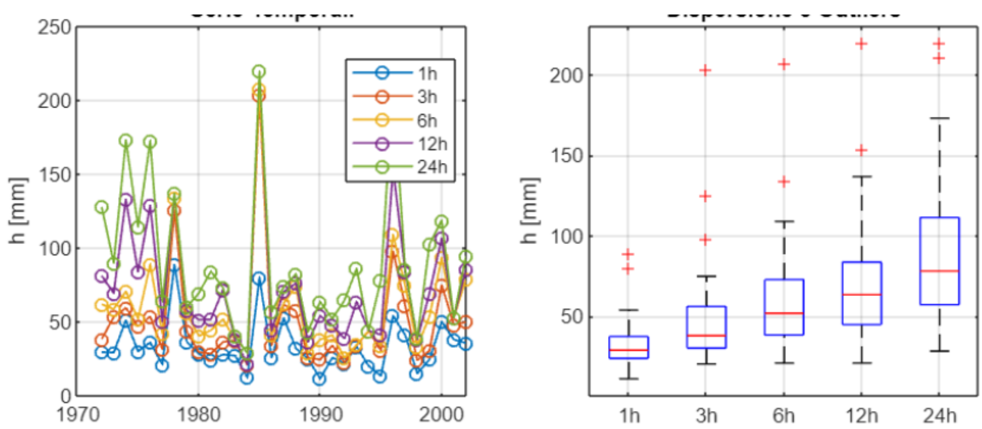

Figure 3: Annual maximum precipitation time series (left) and boxplot outlier dispersion analysis (right) for standard rainfall durations across the historical record.

To model the probability of exceedance, we tested several theoretical probability density functions, focusing primarily on those suited for extreme values. While the Method of Moments (MOM) is traditional, we also considered L-moments for their robustness against outliers [8]. The sample L-moments λ_r are linear combinations of probability-weighted moments (PWMs), defined as:

$$\beta_r = E\left[X\{F(X)\}^r\right] \tag{7}$$

where $F(X)$ is the cumulative distribution function. The first two L-moments, representing the mean and a measure of scale (L-scale), are simply $\lambda_1 = \beta_0$ and $\lambda_2 = 2\beta_1 - \beta_0$. From these, we compute the L-skewness (τ_3) and L-kurtosis (τ_4) coefficients, which provide a unbiased estimation of the distribution tail behavior:

$$\tau_3 = \frac{\lambda_3}{\lambda_2}, \quad \tau_4 = \frac{\lambda_4}{\lambda_2} \tag{8}$$

Our comparative analysis evaluated the Lognormal (two-parameter), Gumbel (Extreme Value Type I), and Generalized Extreme Value (GEV) distributions. Goodness-of-fit was measured using the Kolmogorov-Smirnov (KS) test, which assesses the maximum absolute difference between the empirical ($F_m(x)$) and theoretical ($F_0(x)$) cumulative distribution functions over the sample size N:

$$D_{max} = \max_{1 \le i \le N} \left| F_0(x_i) - \frac{i-1}{N} \right| \le D_{crit}(\alpha) \tag{9}$$

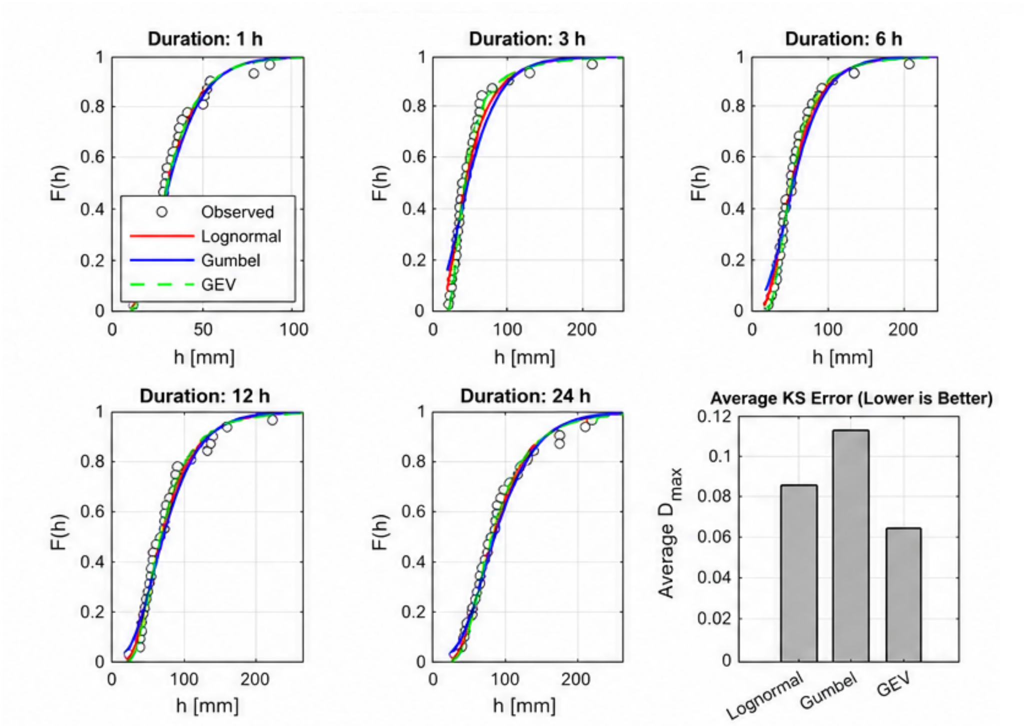

Figure 4: Best-fit probability distributions (Lognormal, Gumbel, GEV) for extreme rainfall data across standard operational durations and the corresponding Average Kolmogorov-Smirnov (KS) error calculation graph.

Ultimately, the Gumbel (EV1) and GEV models provided the most robust fit for the Mediterranean context of our study area [7]. The cumulative distribution function for the Gumbel law, expressing the non-exceedance probability $P(x)$, is standardly defined as:

$$P(x) = \exp\left\{ -\exp\left[-\frac{x - u_d}{\alpha_d} \right] \right\} \tag{10}$$

where α_d is the scale parameter (affecting the spread of the distribution) and u_d is the location parameter (representing the mode), both of which vary depending on the rainfall duration d [3]. These parameters are related to the L-moments via:

$$\alpha_d = \frac{\lambda_2}{\ln(2)} \tag{11}$$

$$u_d = \lambda_1 - \gamma \cdot \alpha_d \tag{12}$$

where $\gamma \approx 0.5772$ is the Euler-Mascheroni constant. By inverting the CDF for a target return period T, where $P(x) = 1 - 1/T$, we extract the baseline design quantile $h_{ref,d,T}$:

$$h_{ref,d,T} = u_d - \alpha_d \cdot \ln\left[-\ln\left(1 - \frac{1}{T}\right)\right] \tag{13}$$

2.3 Applying Climate Change Adaptation Factors

Relying solely on historical data implies a belief in climate stationarity. In light of modern climatology, this is a dangerous assumption. Warmer atmospheric conditions increase the water-holding capacity of the air (following the Clausius-Clapeyron relation by approximately 7% per degree of warming), leading to more intense, localized precipitation bursts.

To prevent our infrastructure designs from being obsolete upon completion, we corrected the baseline precipitation quantiles. We achieved this by applying specific Adaptation Factors (F_A) derived from regional climate models downscaled for Sicily [13]. We focused on the "Near Future" scenario (typically covering the period 2023-2050), which provides a realistic planning horizon for municipal engineering works.

The future design rainfall depth $h_{fut,d,T}$ for a specific duration d and return period T is calculated via a straightforward linear adjustment:

$$h_{fut,d,T} = h_{ref,d,T} \cdot F_A(d, T, \text{Scenario}) \tag{14}$$

The factor F_A is not a single constant; it varies based on the return period and the specific duration of the event. Generally, shorter-duration events exhibit a higher F_A, meaning flash floods will become disproportionately more severe than longer, multi-day rainfall events. This non-uniform scaling behavior is operationalized via a matrix layout of the adaptation parameter, summarized in Table 1.

Table 1: Conceptual Framework for Time-and-Frequency Dependent Adaptation Factors (F_A)

Rainfall Duration (d)	**Tr = 50 Years**	**Tr = 100 Years**	**Tr = 300 Years**
Sub-hourly / Convective (< 1 h)	$F_{A,max}$ ($\approx 1.25 - 1.35$)	F_A ($\approx 1.22 - 1.30$)	F_A ($\approx 1.18 - 1.25$)
Short / Torrential (1 – 3 h)	F_A ($\approx 1.18 - 1.22$)	F_A ($\approx 1.15 - 1.18$)	F_A ($\approx 1.12 - 1.15$)
Intermediate (6 – 12 h)	F_A ($\approx 1.10 - 1.15$)	F_A ($\approx 1.08 - 1.12$)	F_A ($\approx 1.05 - 1.10$)
Long / Frontal (24 h)	$F_{A,min}$ ($\approx 1.05 - 1.08$)	F_A ($\approx 1.03 - 1.05$)	F_A ($\approx 1.00 - 1.03$)

This adjustment is arguably the most critical step in transitioning from a traditional hydrological study to a forward-looking, climate-resilient hazard assessment. The resulting mathematical DDF model incorporates this amplification directly into its core regression, modifying the power-law parameters:

$$h_{fut}(t, T) = [F_A \cdot a(T)] \cdot t^{n_{cc}} \tag{15}$$

where n_{cc} represents the climate-adjusted scaling exponent, accounting for the steeper attenuation typical of short, high-energy convective bursts.

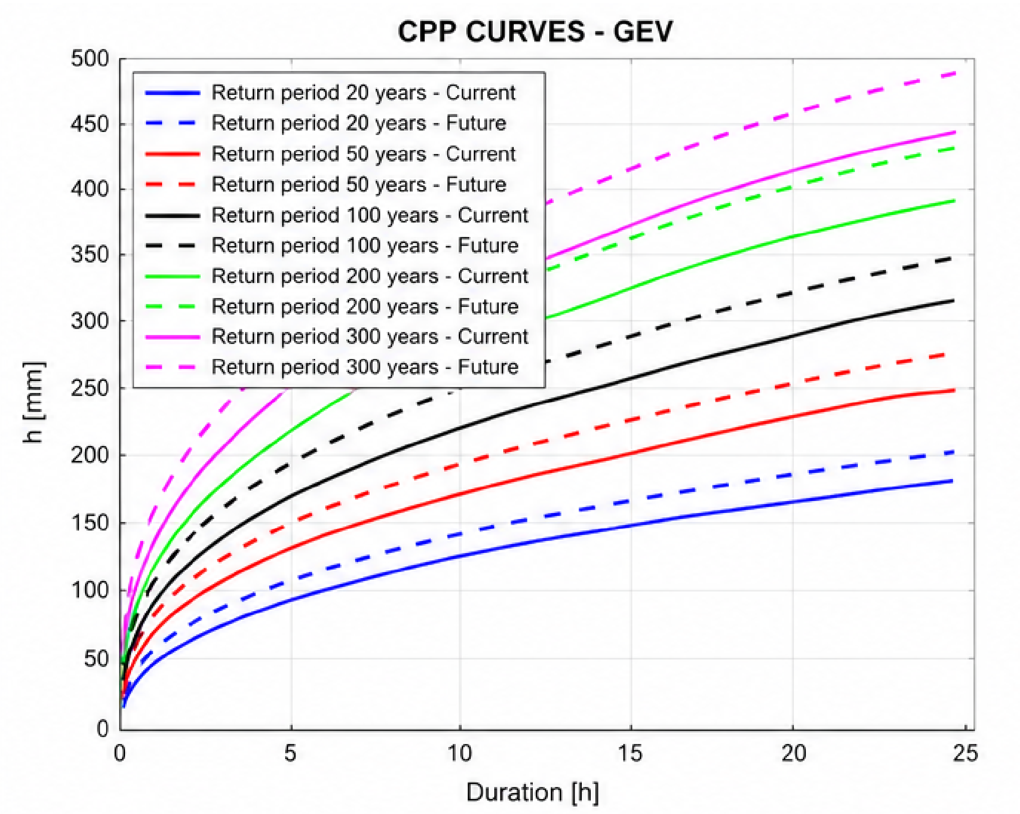

Figure 5: Climate-adjusted Depth-Duration-Frequency (DDF) probability curves mapped under the GEV model comparing current baseline data and future climate projections.

2.4 Time of Concentration Assessment

To properly frame the watershed's temporal dynamic, we focused on the time of concentration (t_c), defined as the time required for a drop of water to travel from the hydraulically most remote point of the basin to the closing section. Given the high sensitivity of peak discharge to this parameter, we implemented an ensemble approach to avoid the single-formula bias inherent to ungauged catchment modeling [11]. t_c was calculated using an average of four methods well-calibrated for small, steep Italian catchments: Giandotti, Pezzoli, Ventura, and Viparelli.

The formulation architecture for each of these selected methods is structured as follows:

1. **Giandotti Method:** Explicitly considers the macro-morphology of the basin, its total drainage surface, and its structural relief profile:

$$t_c^G = \frac{4\sqrt{A} + 1.5L}{0.8\sqrt{Z_{max} - Z_{min}}} \tag{16}$$

where A is the drainage area (km^2), L is the main channel length (km), and Z_{max}, Z_{min} are the boundary elevations (m a.s.l.).

2. **Ventura Method:** Calibrated specifically for steep, unchannelized mountain catchments, establishing a direct correlation with the average geometric slope of the primary drainage line:

$$t_c^V = \frac{7.6 \cdot \sqrt{A}}{\sqrt{i_m}} \tag{17}$$

where i_m is the mean channel slope (m/m).

3. **Pezzoli Method:** Integrates a cinematic approximation derived from uniform flow equations under structural slope conditions, accounting for the hydraulic shape factor (A/L^2):

$$t_c^P = \frac{L}{2 \cdot \sqrt{g \cdot \Delta H}} \cdot \left(\frac{A}{L^2}\right)^{0.25} \tag{18}$$

where $g = 9.81$ m/s^2 is the acceleration due to gravity and $\Delta H = Z_{max} - Z_{min}$ is the total relief drop.

4. **Viparelli Method:** Utilizes a cinematic wave propagation scheme assuming a reference average velocity ($v_m \approx 1.5 - 2.0$ m/s) calibrated for mountainous

and highly responsive torrent networks:

$$t_c^W = \frac{L}{3.6 \cdot v_m} \tag{19}$$

The final ensemble time of concentration is computed as the arithmetic mean of the individual formulations to ensure predictive stability and smooth localized formulation bias:

$$t_{c,\text{ensemble}} = \frac{t_c^G + t_c^V + t_c^P + t_c^W}{4} \tag{20}$$

The calculated temporal baselines ensure that the subsequently generated synthetic hyetographs (such as Chicago or alternating block profiles) are perfectly tuned to the critical response window of the river network and its responsive tributaries. A storm event duration exactly matching $t_{c,\text{ensemble}}$ maximizes the overlapping contribution of the whole catchment area at the closing section, yielding the absolute worst-case peak discharge configuration for the hydrodynamic routing mesh.

2.5 Geomorphometry and Kinematic Response

Understanding how a basin translates rainfall into runoff requires a deep dive into its morphometry. The main basin is characterized by a severe topographic gradient. It drops from a maximum elevation of $Z_{max} = 1228$ m down to a closing section at just $Z_{min} = 14$ m above sea level. This massive drop over a relatively short main channel length ($L = 14.5$ km) guarantees rapid flow convergence and minimal rolling effects along the flood plains.

To properly isolate the spatial distribution of risk, the morphometric extraction process was extended to all critical sub-basins intersecting the target urban nodes: Canalicchio, Belvedere, and Pintarca. Table 2 provides the structural geomorphological dataset extracted via GIS processing.

Table 2: Detailed Morphometric and Elevation Data Across the Catchments

Parameter	**Sym.**	**Pint.**	**Belv.**	**Canal.**	**Main**
Drainage Area	A [km^2]	1.14	0.76	3.11	39.00
Main Stream Length	L [km]	2.50	2.00	4.10	14.50
Max Elevation	Z_{max} [m]	409.6	261.0	409.6	1228.0
Min Elevation	Z_{min} [m]	72.0	20.0	72.0	14.0
Mean Elevation	Z_{med} [m]	240.8	140.5	240.8	621.0
Total Elevation Drop	ΔH [m]	337.6	241.0	337.6	1214.0
Mean Channel Slope	i_m [m/m]	0.14	0.12	0.08	0.08
Shape Factor	A/L^2 [−]	0.18	0.19	0.18	0.19

Running the four-method ensemble calculation framework across these physical inputs revealed a steep temporal polarization between the main collector and its headwater zones. The results of this specific temporal calibration are documented in Table 3.

Table 3: Ensemble Calculations for Time of Concentration (t_c)

Catchment	**Giandotti [h]**	**Ventura [h]**	**Pezzoli [h]**	**Viparelli [h]**	**Mean t_c [h]**
Pintarca	0.77	0.37	0.37	0.69	**0.55**
Belvedere	0.74	0.32	0.32	0.56	**0.48**
Canalicchio	1.27	0.78	0.79	1.14	**0.99**
Main Basin	2.37	2.75	2.76	4.03	**2.98**

Our computations yielded an average t_c of approximately 2.98 hours for the entire basin. However, the true operational danger lies in the sub-basins. For instance, the Pintarca tributary, heavily constrained and steeply sloped, exhibited a frighteningly short concentration time of just 0.55 hours (33 minutes). This metric alone underscores the intense flash-flood potential that threatens the localized urban clusters built along its banks, providing almost zero physical attenuation buffer during high-intensity cloudbursts.

2.6 Runoff Generation via the SCS-CN Method

Not all rainfall reaches the river network. To separate gross precipitation into infiltration losses and effective surface runoff, we employed the Soil Conservation Service Curve Number (SCS-CN) method [10]. This empirical model is highly effective for ungauged basins because it relies on observable physical characteristics rather than historical streamflow gauge data.

Using QGIS, we performed a spatial intersection between the Corine Land Cover maps (defining land use patterns and vegetative cover densities) and regional geological maps (defining the Hydrologic Soil Group, classified from A to D based on structural transmission rates and minimum infiltration capacities). Group B (moderate infiltration) and Group C (slow infiltration rates due to clayey-loam substrates) dominate the mountain sectors. Area-weighted averaging across the watershed resulted in a composite Curve Number (CN) of 78 under average antecedent moisture conditions (AMC II).

The potential maximum soil retention S (expressed in millimeters) is mathematically derived from the Curve Number:

$$S = 254 \cdot \left(\frac{100}{CN} - 1 \right) \tag{21}$$

For $CN = 78$, the baseline storage capability equals $S = 71.64$ mm. The method assumes an initial abstraction I_a, representing interception by vegetation, surface depression storage, and initial infiltration before runoff begins. Standard regional engineering practice sets $I_a = 0.2S$, which yields $I_a = 14.33$ mm. Consequently, the net effective rainfall P_{net} generated during a storm event of total depth P is given by:

$$P_{net} = \frac{(P - I_a)^2}{P - I_a + S} \quad \text{for} \quad P > I_a \tag{22}$$

When analyzing extreme events associated with climate change, one must consider that heavy convective storms often hit already saturated ground due to antecedent multi-day precipitation fronts. If we shift the evaluation baseline to a wet condition (AMC III), the curve number increases drastically. The non-linear conversion from AMC II to AMC III is operationalized via the following expression:

$$CN_{III} = \frac{CN_{II}}{0.427 + 0.00573 \cdot CN_{II}} \tag{23}$$

Applying this formulation for a baseline $CN_{II} = 78$ increases the runoff rating to $CN_{III} = 89.2$. The maximum retention capacity correspondingly collapses to $S_{III} = 30.7$ mm, and the initial abstraction drops to $I_{a,III} = 6.1$ mm. This non-linear relationship demonstrates how saturated soils completely lose their buffering capacity, turning almost the entirety of a climate-amplified rainfall spike directly into dangerous surface runoff [1].

Table 4 tracks the final evaluation of total design rainfall vs. effective net runoff across the three reference return periods ($T_r = 50, 100, 300$ years) comparing the historical baseline with the climate-amplified projection (F_A).

Table 4: Rainfall-Runoff Transformation via SCS-CN Method

	Tr = 50y		**Tr = 100y**		**Tr = 300y**	
Variable [unit]	Base	Clim	Base	Clim	Base	Clim
Gross Rainfall P [mm]	78.5	96.6	91.2	110.4	109.4	130.2
Initial Abstr. I_a [mm]	14.3	14.3	14.3	14.3	14.3	14.3
Soil Retention S [mm]	71.6	71.6	71.6	71.6	71.6	71.6
Net Rainfall P_{net} [mm]	30.5	43.8	40.2	54.4	53.6	70.9
Runoff Coeff. C [−]	0.39	0.45	0.44	0.49	0.49	0.55

The drastic increase in the global runoff coefficient ($C = P_{net}/P$), which rises from 0.388 to 0.545, clearly reflects the highly non-linear nature of watershed physics. As rainfall depths increase due to climate change, the soil retention threshold represents an increasingly smaller fraction of the total volume, triggering an exponential surge in peak flow generation.

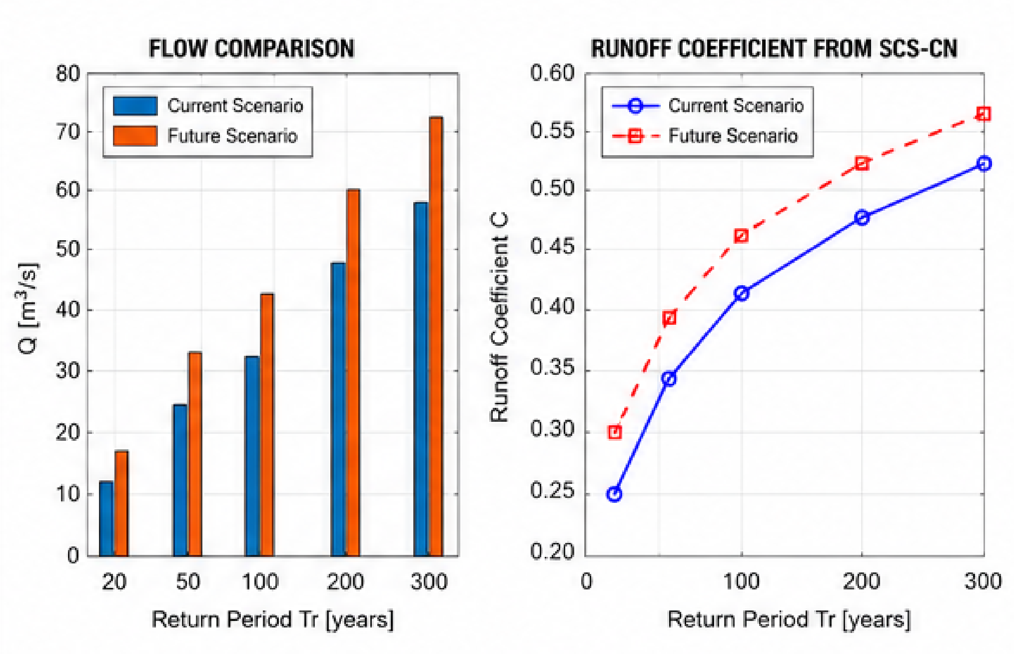

Figure 6: Hydrodynamic comparison of peak flow discharge rates (left) and the non-linear increase of the SCS-CN runoff coefficient C (right) between the current operational baseline and the future climate scenario.

With the net rainfall hyetographs defined, we utilized a kinematic routing approach to generate the final design flood hydrographs.

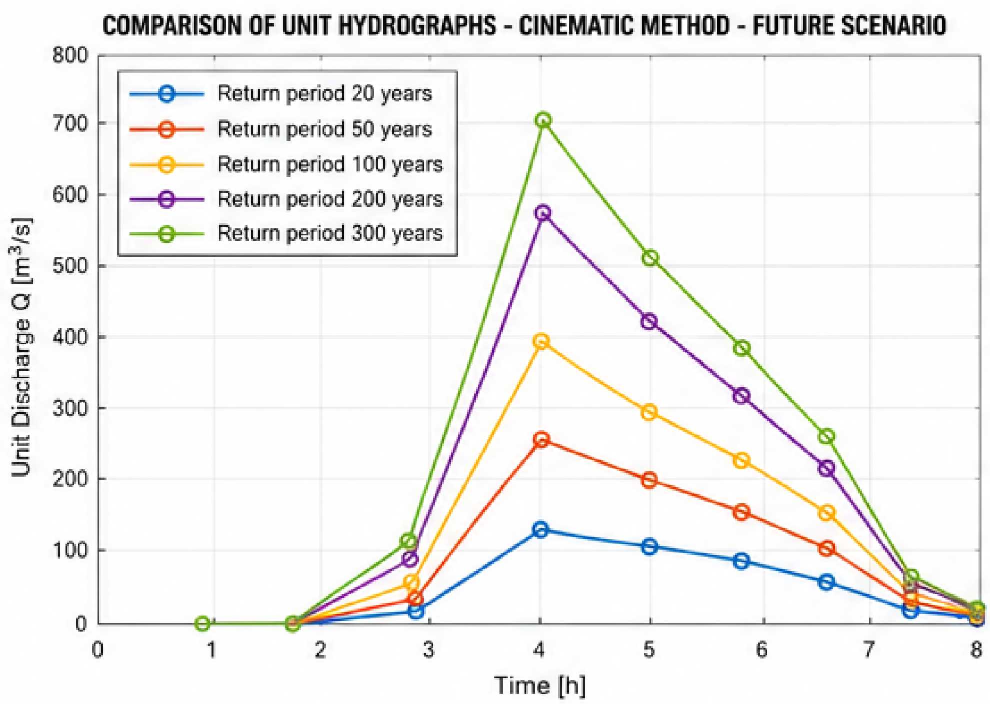

Figure 7: Design net flood hydrographs simulated across multiple return periods (T_r) utilizing the climate-adjusted kinematic wave method.

3 Two-Dimensional Hydrodynamic Routing

Hydrological models provide the volume and timing of water arriving at a specific section, but they tell us nothing about what happens when that water spills out of the river channel and interacts with roads, buildings, and retaining walls. For this spatial assessment, we deployed the HEC-RAS 2D modeling engine [2].

Traditional approaches that simplify floodplain flow to one-dimensional streams fail to capture the multi-directional velocity vectors typical of alluvial plains and dense urban settlements. The conversion of a localized hydrograph spike into physical depths and velocities requires a distributed mathematical framework capable of routing dynamic waves over arbitrary topography.

3.1 Governing Equations: 2D Shallow Water Formulation

HEC-RAS 2D operates by numerically solving the 2D depth-averaged Shallow Water Equations (SWE), also known as the Saint-Venant equations in two dimensions. Because the horizontal dimensions of the floodplain are orders of magnitude larger than the water depth, the vertical velocity components and vertical accelerations can be safely neglected. Consequently, the pressure distribution is assumed to be strictly hydrostatic throughout the computational domain.

The mathematical framework consists of a mass conservation (continuity) equation coupled with two momentum conservation equations mapped along the orthogonal Cartesian axes (x and y). The continuity equation is formulated as follows:

$$\frac{\partial H}{\partial t} + \frac{\partial (hu)}{\partial x} + \frac{\partial (hv)}{\partial y} = q \tag{24}$$

where $H(x, y, t)$ is the absolute water surface elevation (m a.s.l.), $h(x, y, t)$ is the local water depth (m), u and v are the depth-averaged velocity components along the x and y directions respectively (m/s), and q represents the volumetric source/sink term per unit area (m/s), which accounts for localized direct rainfall forcing, net infiltration losses, or structural lateral point-source inflows.

The conservation of momentum in the x-direction is given by a partial differential formulation that accounts for local acceleration, convective transport, hydrostatic pressure gradients, gravity, bottom friction, and turbulent mixing:

$$\frac{\partial u}{\partial t} + u\frac{\partial u}{\partial x} + v\frac{\partial u}{\partial y} = -g\frac{\partial H}{\partial x} + \nu_t\left(\frac{\partial^2 u}{\partial x^2} + \frac{\partial^2 u}{\partial y^2}\right) - c_f u + f_c v \tag{25}$$

Similarly, the conservation of momentum along the y-axis is defined as:

$$\frac{\partial v}{\partial t} + u\frac{\partial v}{\partial x} + v\frac{\partial v}{\partial y} = -g\frac{\partial H}{\partial y} + \nu_t\left(\frac{\partial^2 v}{\partial x^2} + \frac{\partial^2 v}{\partial y^2}\right) - c_f v - f_c u \tag{26}$$

where g is the gravitational acceleration (9.81 m/s^2). The parameter f_c represents the Coriolis acceleration factor, which can be neglected in localized catchment analysis but remains present in the global solver formulation. The term ν_t represents the horizontal eddy viscosity coefficient (m^2/s), which is critical for modeling the turbulent kinetic energy dissipation and macro-eddies that develop when torrential flows hit urban obstacles. HEC-RAS evaluates ν_t utilizing a combined Smagorinsky and parabolic formulation:

$$\nu_t = D \cdot u_* \cdot h + C_s^2 \cdot \Delta x^2 \cdot \sqrt{2\left(\frac{\partial u}{\partial x}\right)^2 + \left(\frac{\partial u}{\partial y} + \frac{\partial v}{\partial x}\right)^2 + 2\left(\frac{\partial v}{\partial y}\right)^2} \tag{27}$$

where D is the mixing coefficient, $u_* = \sqrt{ghS_f}$ is the shear velocity, and C_s is the Smagorinsky constant (≈ 0.2). The bottom friction coefficient c_f (s^{-1}) is intrinsically tied to the empirical Manning's roughness coefficient (n) via the hydraulic relationship:

$$c_f = \frac{gn^2\sqrt{u^2 + v^2}}{h^{4/3}} \tag{28}$$

For specific areas characterized by low-velocity gradients and gradually varied subcritical flows, HEC-RAS allows the selection of the Shallow Water Diffusion Wave equations (DSW). The DSW framework discards the local and convective acceleration terms from the momentum balance, reducing the system to a equilibrium between the hydrostatic pressure force, gravity, and bottom friction:

$$g\nabla H + \mathbf{S_f} = 0 \implies S_{f,x} = -\frac{\partial H}{\partial x}, \quad S_{f,y} = -\frac{\partial H}{\partial y} \tag{29}$$

While the DSW solver is computationally faster and highly stable, the full SWE solver was enforced across the Torrente Muto simulation. This choice was necessary because flash floods in highly urbanized Mediterranean catchments feature rapid velocity transitions, hydraulic jumps, and sudden momentum changes around structural bottlenecks that would be heavily smoothed by the diffusion approximation [4].

3.2 Topographic Discretization: DTM and Computational Mesh

The accuracy of a 2D hydrodynamic model is strictly bound by the quality of the underlying terrain data. We utilized a high-resolution Digital Terrain Model (DTM) derived from airborne LiDAR flights, providing an exceptional 1×1 meter spatial resolution.

However, raw DTMs often struggle to accurately capture sharp hydraulic features, especially in densely vegetated or urbanized riverbeds. We spent considerable effort in QGIS performing hydro-enforcement on the DTM, "burning in" culverts beneath roads and smoothing out artificial digital dams that might artificially hold back water in the simulation.

Over this terrain, we draped the 2D computational mesh. HEC-RAS 2D allows for an unstructured, polygonal mesh featuring sub-grid bathymetry. This means that while a computational cell might have a large surface area, the software extracts detailed elevation-volume and cross-sectional area data from the underlying 1×1 m DTM for the cell faces.

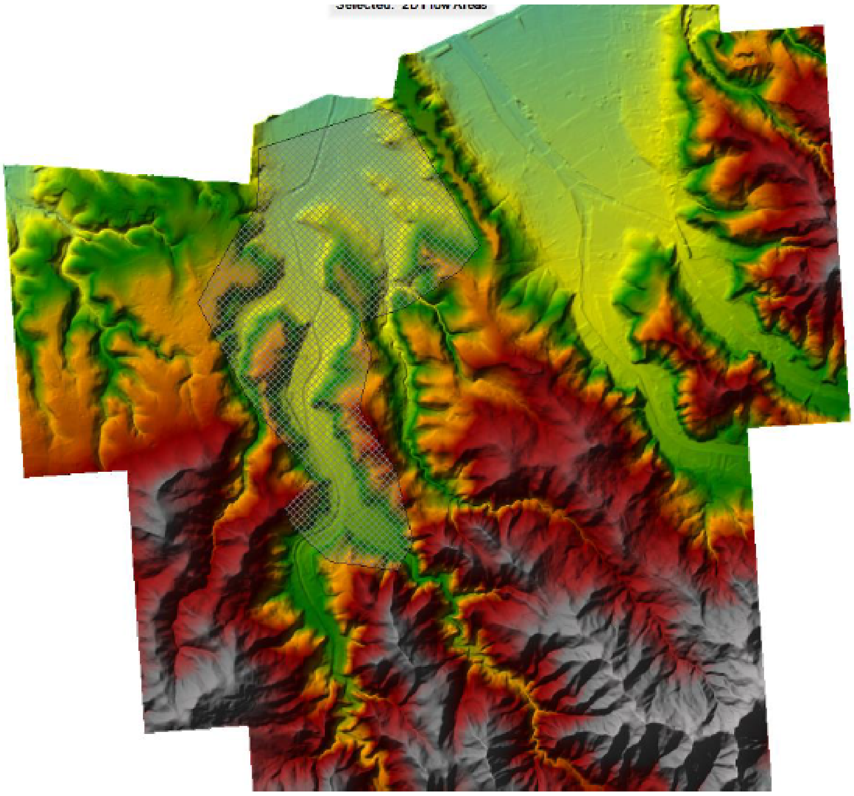

Figure 8: Visualization of the high-resolution unstructured 2D computational mesh, meticulously mapped over the hydro-enforced LiDAR DTM within the HEC-RAS environment.

The sub-grid bathymetric framework relies on pre-calculating geometric property tables for each computational cell and face before launching the hydraulic solver. Instead of using a single average elevation for a large cell, the algorithm samples the fine-resolution DTM inside the cell boundary to construct a continuous hydraulic capacity function. The mathematical relationships governing cell volume and face capacity are defined as:

$$\Omega_i(H) = \iint_{A_i} \mathcal{H}(H - z(x, y))\, dxdy \tag{30}$$

$$A_f(H) = \int_{L_f} \mathcal{H}(H - z_f(s)) \cdot (H - z_f(s))\, ds \tag{31}$$

where $\Omega_i(H)$ is the storage volume available in cell i at water level H, $A_f(H)$ is the flow area through cell face f, $z(x, y)$ is the LiDAR terrain elevation, L_f is the linear profile of the face, and $\mathcal{H}$ is the Heaviside step function. This mathematical approach allows large computational blocks to pass flow based on the actual micro-topography of the terrain, preventing artificial blockages without requiring a prohibitively expensive micro-mesh.

To strike an optimal balance between computational efficiency and hydraulic precision—particularly around critical infrastructures like bridges and channel meanders—the mesh was refined using spatial breaklines. We defined a maximum triangular cell area of 5 m^2 in the floodplains, tightening down to a minimum of 1 m^2 directly within the main channel and near constriction points.

3.3 Parameterization and Stability

Manning's roughness coefficient (n) was spatially distributed across the mesh based on Corine Land Cover data. We assigned a base value of $n = 0.033$ s/m$^{1/3}$ for the main channel bed (typical of moderately clean, winding channels with some stones and weeds). The floodplains received higher values (ranging from 0.05 to 0.12 s/m$^{1/3}$) to simulate the immense hydraulic drag exerted by thick riparian vegetation, fences, and dense urban housing blocks [6]. Table 5 summarizes the spatial calibration matrix enforced across the computational domain.

Table 5: Spatial Distribution of Manning's Roughness Coefficients (n)

Land Use Class	n **[s/m$^{1/3}$]**	**Hydraulic Classification**
Main Channel Bed	0.033	Clean, winding natural stream
Dense Riparian Woods	0.120	Heavy timber, dense undergrowth
Shrubland / Scrub	0.065	Medium to dense brush
Agricultural Parcels	0.045	Mature crops, minimal tillage
Discont. Urban Fabric	0.080	Gardens, fences, obstacles
Cont. Urban Matrix	0.150	Impervious, severe building drag
Paved Infrastructure	0.016	Smooth asphalt, rapid transport

To ensure the mathematical stability of the finite volume solver during the dynamic simulation, the computational time step (Δt) must be carefully selected in relation to cell size (Δx) and flow velocity (V). We adhered strictly to the Courant-Friedrichs-Lewy (CFL) condition, monitoring the Courant number C:

$$C = \frac{V \cdot \Delta t}{\Delta x} \leq 1.0 \tag{32}$$

When operating under the full SWE solver, the celerity of the gravity wave ($c = \sqrt{gh}$) must be accounted for alongside the physical advective flow velocity. This modifies the numerical criteria into an absolute wave Courant condition:

$$C_{wave} = \frac{\left(\sqrt{u^2 + v^2} + \sqrt{gh}\right) \cdot \Delta t}{\Delta x} \leq 1.0 \tag{33}$$

Given the average minimum grid size ($\Delta x \approx 1.0-2.0$ m) enforced along the urban channels and the high velocities ($V > 3.5$ m/s) reached during the climate-amplified $T_r = 300$ years simulation, the computational time step was dynamically restricted using an adaptive time-stepping routine. The boundary operational variables for the numerical integration loops are detailed in Table 6.

Table 6: HEC-RAS 2D Computational Solver Settings

Numerical Parameter	**Value/Selection**	**Unit**
Hydrodynamic Equation Set	Full SWE	–
Theta Implicit Factor	1.00	–
Max Courant Number (C_{max})	1.00	–
Min Courant Number (C_{min})	0.45	–
Initial Time Step	0.50	s
Adaptive Time Step Range	0.05 – 1.00	s
Water Surface Tolerance	0.003	m
Volume Check Tolerance	0.001	m
Max Iterations per Step	20	–

By keeping the Courant number near or below 1.0, we avoided numerical diffusion and ensured that the simulated flood wave did not physically "skip" across multiple computational cells in a single time step, which would have compromised the integrity of the hazard outputs.

4 Hazard Classification and Urban Planning

The ultimate objective of running hours of computationally heavy SWE simulations is not just to generate impressive graphics; it is to create legally binding maps that protect human life and guide territorial development.

Once the simulations concluded for the various design return periods ($T_r = 50, 100, 300$ years), HEC-RAS yielded continuous spatial grids containing the maximum water depth (H) and maximum flow velocity (v) for every square meter of the domain.

However, raw depth and velocity numbers are difficult for city planners and politicians to interpret directly. We needed to translate these hydrodynamic variables into categorical Hazard Zones according to institutional directives (such as the Italian PAI - Piano di Assetto Idrogeologico).

The hazard level is generally a function of the flow's specific energy and its capacity to sweep away pedestrians or damage structures. A common proxy for this destructive force is the depth-velocity product ($H \times v$). Using QGIS Raster Calculator, we processed the raw output maps through a decision matrix. The territory was segmented into four distinct hazard classes: * **P1 (Low Hazard):** Areas experiencing shallow flooding ($H < 0.3$ m) and low velocities. Typically manageable nuisance flooding. * **P2 (Moderate Hazard):** Water depths between 0.3 m and 1.0 m. Dangerous for children and vehicles, but manageable for healthy adults. * **P3 (High Hazard):** Depths exceeding 1.0 m or high velocities. Significant structural damage is possible; evacuation is difficult. * **P4 (Very High Hazard):** Areas where the hydraulic head H exceeds 2 meters, or where torrential velocities combined with depths greater than 1 meter occur. Total destruction of light structures is probable, and human survival without immediate rescue is unlikely.

For our study, the 300-year return period event (amplified by climate change factors) served as the benchmark for defining the most restrictive P3 and P4 zones.

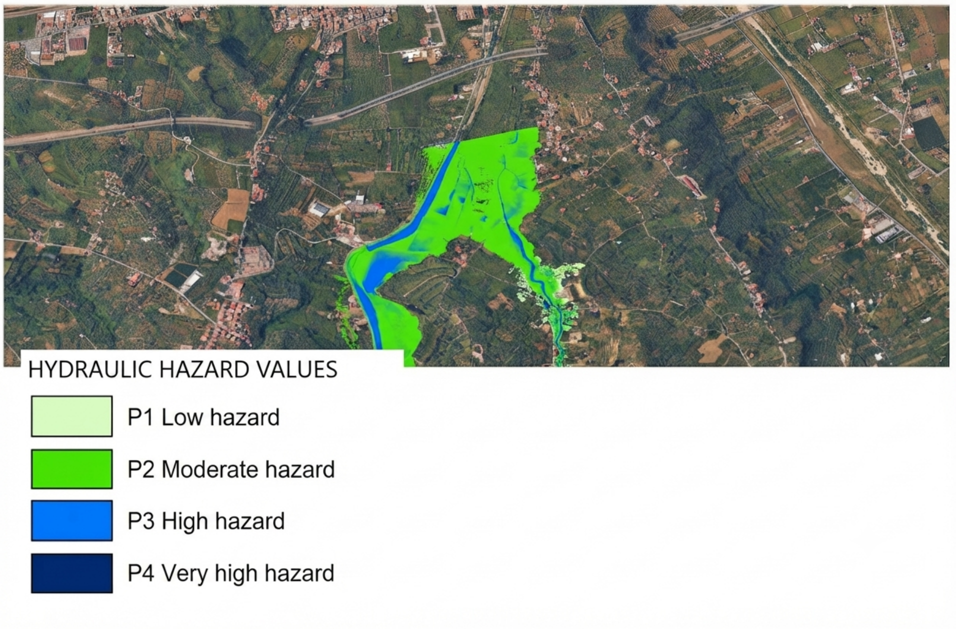

Figure 9: Final comprehensive Hydraulic Hazard Map processed at a 1:25,000 regulatory scale, highlighting flood vectors, attention areas, and safety perimeters mapped over GIS layers.

These maps cease to be merely scientific exercises and become rigorous regulatory tools. A P4 classification places an immediate legal embargo on any new residential or commercial construction. Furthermore, it mandates that local authorities implement active mitigation strategies—such as detention basins, levee reinforcements, or strategic managed retreat—and requires rigorous flood-proofing for existing critical infrastructure (hospitals, power substations) caught within the perimeter. Any proposed development in adjacent P1 or P2 zones must strictly prove "hydraulic invariance," ensuring that new impermeable surfaces do not exacerbate the risk profile for downstream neighbors.

5 Conclusions

Engineering practices rooted purely in the historical past are dangerously ill-equipped to handle the future. Adapting our hydraulic safety standards to accommodate the reality of climate change is no longer optional; it is an absolute technical and ethical necessity.

Through the extensive application of this modern framework to the Torrente Muto basin and its steep tributaries, we demonstrated that standard assumptions fall short. By tightly integrating climate-adjusted rainfall models (via regional adaptation factors), rigorous SCS-CN runoff mechanics, and sub-grid 2D hydrodynamic routing, we generated a hazard assessment that is vastly more representative of actual flood physics than older, stationary 1D methodologies.

The granular, high-resolution hazard maps produced by this workflow provide municipal administrations and civil protection agencies with a solid, data-driven, and legally defensible foundation for action. They allow decision-makers to prioritize infrastructural interventions, secure vulnerable populations, and enforce logical building constraints.

Looking forward, this methodology is highly scalable. The next evolutionary step for this research involves multi-hazard coupling. Mediterranean basins are rarely subjected to clear-water floods alone. Future modeling efforts should integrate sediment transport equations and non-Newtonian rheological models to simulate the devastating impacts of mudflows, debris flows, and massive solid transport on the already limited hydraulic capacity of these vital drainage networks.

References

[1] A. Brath, A. Montanari, and G. Moretti. Assessing the effect of land-use changes on annual streamflow using a hydrological model. *Journal of Hydrology*, 326:122–143, 2006.

[2] G. W. Brunner. *HEC-RAS River Analysis System, 2D Modeling User's Manual*. US Army Corps of Engineers, Hydrologic Engineering Center (CEIWR-HEC), 2020.

[3] V. T. Chow, D. R. Maidment, and L. W. Mays. *Applied Hydrology*. McGraw-Hill, 1988.

[4] P. Costabile, F. Macchione, L. Natale, and G. Petaccia. Enhancing river model set-up for 2d dynamic flood modelling. *Environmental Modelling & Software*, 67:89–107, 2015.

[5] A. Cuomo and D. Guida. Hydro-geomorphologic-based water budget at event time-scale in a mediterranean headwater catchment. *Hydrology*, 8(1), 2021.

[6] M. Diakakis, G. Deligiannakis, K. Katsetsiadou, and E. Lekkas. Flash flood hazard mapping in a mediterranean urbanized catchment. *Science of the Total Environment*, 575:1202–1213, 2017.

[7] A. Forestieri, F. Lo Conti, S. Blenkinsop, H. J. Fowler, and L. V. Noto. Regional frequency analysis of extreme rainfall in sicily (italy). *International Journal of Climatology*, 38(11):4036–4054, 2018.

[8] J. R. M. Hosking. L-moments: Analysis and estimation of distributions using linear combinations of order statistics. *Journal of the Royal Statistical Society: Series B (Methodological)*, 52(1):105–124, 1990.

[9] IPCC. *Climate Change 2021: The Physical Science Basis. Contribution of Working Group I*. Cambridge University Press, 2021.

[10] S. K. Mishra and V. P. Singh. Soil conservation service curve number (scs-cn) methodology. *Water Science and Technology Library*, 42, 2003.

[11] Biagio Saya. Automated gis-based hydrological modeling framework for flood hydrograph estimation in ungauged mediterranean catchments. 2026.

[12] Biagio Saya. Development of hydraulic hazard mapping within a gis environment: Interoperability between hec-ras and qgis. 2026.

[13] D. Treppiedi, A. Francipane, and L. V. Noto. Assessment of rainfall probability curves for the 21st century in sicily. *Proceedings of IDRA 2024*, 2024.